Density of states and Fisher's zeros in compact U(1) pure gauge theory

A. Bazavov, B. A. Berg, Daping Du, and Y. Meurice

Phys. Rev. D **85**, 056010 — Published 30 March 2012

DOI: 10.1103/PhysRevD.85.056010

BNL-96917-2012-JA

Density of states and Fisher's zeros in compact $U(1)$ pure gauge theory

A. Bazavov
Department of Physics
Brookhaven National Laboratory
Upton, NY 11973, USA

B. A. Berg
Department of Physics
Florida State University
Tallahassee, FL 32306, USA

Daping Du
Physics Department
University of Illinois
Urbana, IL 61801, USA

Y. Meurice
Department of Physics and Astronomy
The University of Iowa
Iowa City, Iowa 52242, USA

We present high-accuracy calculations of the density of states using multicanonical methods for lattice gauge theory with a compact gauge group $U(1)$ on 4^4, 6^4 and 8^4 lattices. We show that the results are consistent with weak and strong coupling expansions. We present methods based on Chebyshev interpolations and Cauchy theorem to find the (Fisher's) zeros of the partition function in the complex $\beta = 1/g^2$ plane. The results are consistent with reweighting methods whenever the latter are accurate. We discuss the volume dependence of the imaginary part of the Fisher's zeros, the width and depth of the plaquette distribution at the value of β where the two peaks have equal height. We discuss strategies to discriminate between first and second order transitions and explore them with data at larger volume but lower statistics. Higher statistics and even larger lattices are necessary to draw strong conclusions regarding the order of the transition.

PACS numbers: 11.15.-q, 11.15.Ha, 11.15.Me, 12.38.Cy

I. INTRODUCTION

The ongoing effort at the Large Hadron Collider has trigerred a renewed interest in the phase structure of lattice gauge theory models that may possibly provide an alternative to the Higgs mechanism of the electro-weak symmetry breaking. In particular, the location of the conformal windows for various families of models have stirred intense discussions. Different numerical and analytical techniques have been applied to QCD-like models with large number of fermion flavors [1–6] or with fermions in higher representations [7–12]. An interesting attempt to classify possible phases of such models based on an effective potential for the Polyakov loop was made in [13]. See also [14–16] for recent reviews of results and expectations. Another direction where massive vector bosons emerge without introducing new fermion species but in a model with modified gauge transformations has been pursued in [17, 18].

In this context, it is important to understand the critical behavior of lattice models from as many consistent points of view as possible. Recently, it was proposed to consider complex extensions [19–21] of the framework proposed by Tomboulis [22] to explain confinement from the point of view of the Renormalization Group (RG) approach. A general feature that we observed is that the Fisher's zeros, the zeros of the partition function in the complex β plane [23], play an important role in the determination of the global properties of the complex RG flows. In the case where a phase transition is present, the scaling properties of the zeros [24–29] allow us to distinguish between a first and second order phase transition.

Despite its apparent simplicity, the case of the 4D pure gauge compact $U(1)$ model with a Wilson action is not completely free of controversy. The presence of a double peak for the plaquette distributions near $\beta \simeq 1$ suggests a first order phase transition. However, if spherical or toroidal lattices are considered, the double peak disappears [25, 26]. In addition, finite size scaling, at relatively small volumes seems consistent with a second order phase transition with an exponent $\nu \simeq 0.35 - 0.40$. On the other hand, a possible scenario [30] is that as the volume increases, ν slowly "rolls" towards the first-order value $\nu = 1/D = 0.25$. In the more recent literature [31–34], the idea that the transition is first order is favored. Using finite size scaling, the authors of Ref. [33] estimated the critical value $\beta_\infty = 1.0111310(62)$.

In this article, we introduce new methods to locate the

Fisher's zeros of the the 4D pure gauge compact $U(1)$ model with a Wilson action. We rely on high accuracy determinations of the density of states, a quantity defined in Sec. II, by multicanonical methods [35–38] presented in Sec. III. The lattice sizes considered are 4^4, 6^4 and 8^4. The consistency of the results with weak and strong coupling expansion is checked in Sec. IV. The density of states has a convex region which implies a double peak plaquette distribution near $\beta \simeq 1$. The volume dependence of the double peak distribution is discussed empirically in Sec. V. In Sec. VI, Chebyshev interpolations of the logarithm of the density of states and Cauchy theorem are used to find the Fisher's zeros in the complex $\beta = 1/g^2$ plane. For the lowest zeros, it is possible to check consistency with reweighting methods within error bars estimated from the statistical fluctuations of 20 independent multicanonical streams.

In the following, we use very high statistics on rather small lattices, because this allow us to explore new analysis methods and to test whether they converge faster towards the infinite volume limit. We plan to use similar methods for $SU(2)$ where the imaginary parts of the lowest zeros are larger and reweighting methods become less reliable when the volume increases [39].

Using high statistics at small volumes (4^4, 6^4 and 8^4), we show that the imaginary part of the lowest zero appears to decrease like $L^{-3.08}$, when the linear size L increases from 4 to 8. This could be interpreted as signaling a second-order phase transition with $\nu = 0.325$, a value close to the estimates of Refs. [25, 26]. However, using data at larger volumes but with lower statistics, we found indications for the "rolling" scenario of [30]. This is discussed in Sec. VII where we also consider volume effects on the width and depth of the plaquette distribution at the value of β where the two peaks have equal height. Simulations required to provide a clear cut distinction between first and second order transitions are discussed in the Conclusions.

II. DENSITY OF STATES IN ABELIAN GAUGE THEORY

In the following, we consider the pure gauge partition function

$$Z = \prod_l \int \frac{d\theta_l}{2\pi} \mathrm{e}^{-\beta S} \ , \tag{1}$$

with $\beta \equiv 1/g^2$ and the Wilson action

$$S = \sum_p (1 - \cos\theta_p) \ . \tag{2}$$

We use D dimensional symmetric cubic lattices with L^D sites and periodic boundary conditions. The number of plaquettes is denoted $\mathcal{N}_p \equiv L^D D(D-1)/2$. We define the average action:

$$P \equiv \langle \mathcal{S}/\mathcal{N}_p \rangle = -d(\ln Z/\mathcal{N}_p)/d\beta \ . \tag{3}$$

Inserting 1 as the integral of the delta function over S in Z, we can write

$$Z = \int_0^{2\mathcal{N}_p} dS \ n(S) \ \mathrm{e}^{-\beta S} \ , \tag{4}$$

with the density of states defined as

$$n(S) = \prod_l \int dU_l \delta(S - \sum_p (1 - \cos\theta_p)) \ . \tag{5}$$

Furthermore, we introduce the notation s for $S/\mathcal{N}_p$ and we define the entropy density $f(s)$ via the equation

$$n(S) = \mathrm{e}^{\mathcal{N}_p f(S/\mathcal{N}_p)} \ . \tag{6}$$

A more general discussion for spin models [40] or gauge models [41] can be found in the literature where the density of states is sometimes called the spectral density. From its definition, it is clear that $n(S)$ is positive. Assuming that the measure for the links is normalized to 1, the partition function at $\beta = 0$ is 1. It can be shown [42] that, if the lattice has even number of sites in each direction, and if the gauge group contains $-\mathbb{1}$, then $\beta\cos\theta_p$ goes into $-\beta\cos\theta_p$ by a change of variables $\theta_l \to \theta_l + \pi$ on a set of links such that for any plaquette, exactly one link of the set belongs to that plaquette. Using

$$Z(-\beta) = \mathrm{e}^{2\beta\mathcal{N}_p} Z(\beta) \ , \tag{7}$$

we find the duality

$$n(2\mathcal{N}_p - S) = n(S) \ . \tag{8}$$

This implies the reflection symmetry

$$f(s) = f(2 - s) \ . \tag{9}$$

Numerical values of $f(s)$ have been obtained for discrete values of s between 0 and 1. When s is close to 0 or 2, $f(s)$ diverges logarithmically and we can only reach values of s that are not too close to 0 or 2. Consequently, the results cannot be used if $|\beta|$ is too large. Using the symmetry Eq. (9) and interpolation methods, a continuous function can be obtained in an interval $[\delta, 2 - \delta]$, where δ is an appropriately small quantity.

III. CALCULATION OF THE DENSITY OF STATES

We performed Monte Carlo simulations in pure $U(1)$ gauge theory using Biased Metropolis-Heatbath Updates [37]. To cover a large range of couplings $\beta \in [0, 9]$ we used the multicanonical (MUCA) algorithm [35] with Wang-Landau recursion [36] for the multicanonical weights. The software we used is described in Ref. [38].

We generated large statistics on symmetric lattices with volumes 4^4, 6^4 and 8^4. After the initial recursion we performed three MUCA runs on 4^4, and two runs on

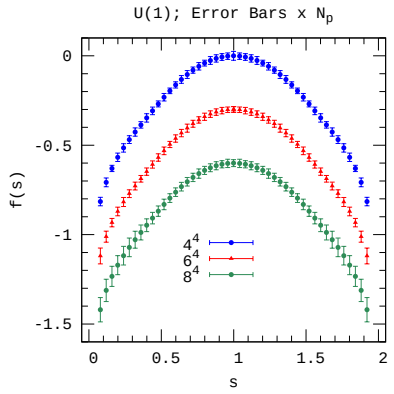

FIG. 1. $f(s)$ on a 4^4 (top) , 6^4 (middle) and 8^4 (bottom) lattices; the errors have been multiplied by $\mathcal{N}_p$; for readability, arbitrary constants have been added to separate the data sets and only one of every 40 points are displayed.

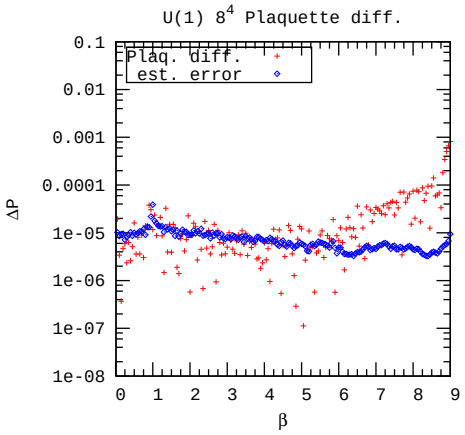

FIG. 2. Difference between the average plaquette calculated with the density of states and directly, for a 8^4 lattice.

6^4 and 8^4. The first MUCA run on 4^4 was regarded as exploratory and we did not include it in the final analysis. The weights for each next run were refined from the previous run. In total we used 20 independent streams for each lattice volume. In each stream we ran Wang-Landau recursion for the multicanonical weights before the production, therefore the weights differ between the streams, $w_{ij}(S)$, where S is the total action, $i = 1, ..., 20$ denotes different streams and $j = 1, 2$ denotes MUCA runs.

The quality of a MUCA run is indicated by the number of tunneling events (*i.e.*, how often during a run the system travels from the lowest energy to the highest and back). Also, to estimate how many statistically independent events we generated, we measured the integrated autocorrelation times. These data are summarized in Appendix A. Our statistics consists of N_{equi} sweeps for equilibration and $N_{rpt} = 64 \times N_{equi}$ sweeps for measurements, where $N_{equi} = 10^6$ for 4^4 and 6^4 lattices and 8×10^5 for 8^4.

For the error analysis we considered two MUCA runs in each stream as independent measurements. Thus, on each lattice we had 40 independent measurements in total. For all quantities in the following the error bars are estimated from an uncorrelated average of these 40 measurements, weighted with the number of tunneling events in each corresponding run, since runs with more tunnelings sample the density of states better. The average results for $f(s)$ are shown in Fig. 1.

To reweight an observable to the canonical ensemble we need to cancel the multicanonical weight $w_{ij}(S)$ and replace it with the Boltzmann factor $\exp(-\beta S)$. For an observable $\mathcal{O}$ of interest, for instance, plaquette, we reweight the time series accumulated during a MUCA run ij to a given coupling β:

$$\langle O\rangle_{ij}(\beta) = \frac{\sum_{k=1}^{N_{rpt}} O_{ij}^k \exp(-\beta S_{ij}^k)/w_{ij}(S_{ij}^k)}{\sum_{k=1}^{N_{rpt}} \exp(-\beta S_{ij}^k)/w_{ij}(S_{ij}^k)}. \qquad (10)$$

The final average is then given as

$$\langle O\rangle(\beta) = \frac{\sum_{i=1}^{20}\sum_{j=1}^{2} N_{ij}^{tunn}\langle O\rangle_{ij}(\beta)}{\sum_{i=1}^{20}\sum_{j=1}^{2} N_{ij}^{tunn}}, \qquad (11)$$

where the number of tunnelings N_{ij}^{tunn} is given in Appendix A.

IV. CONSISTENCY WITH EXISTING RESULTS AND EXPANSIONS

A. Comparison with the average plaquette

As a check of consistency, we compared the average plaquette at various β, as obtained directly from the runs, Eq. (11), and calculated using the average density of states. As shown in Fig. 2, there is a good agreement within the estimated errors.

B. Series for $f(s)$

We compared the numerical results for $f(s)$ with analytical results obtained using the weak and strong coupling expansions. The general methodology has been discussed for $SU(2)$ in [43] and remains applicable here. The basic ingredient is the saddle point equation at s_0:

$$f'(s_0) = \beta \ , \qquad (12)$$

which can be used to convert an expansion of f in powers of s (or $(s-1)^2$) into an expansion of s_0 in powers of $1/\beta$ (or β, respectively). The coefficients of f can then be determined whenever the appropriate expansion of the average plaquette is available. In order to take the finite volume effects into account, we need to include at least the lowest order volume correction, namely

$$P = s_0 + (1/2\mathcal{N}_p)(f'''(s_0)/(f''(s_0))^2) + \mathcal{O}(1/\mathcal{N}_p^2) \ . \qquad (13)$$

Using Eqs. (12) and (13) together with an existing expansion of P including $1/\mathcal{N}_p$ effects up to a certain order, one can determine the coefficients of f up to the corresponding order.

It should also be noted that at finite volume, there is a finite range of β for which f' has a "Maxwellian kink" (discussed in Sec. VII) and three solutions of Eq. (12) are available rather than one. In this region, both expansions are expected to fail. We now proceed to discuss them separately.

C. Strong Coupling

Following Ref. [43], we define

$$g(y) \equiv f(1+y) \equiv \sum_{m=0} g_{2m} y^{2m} \ . \tag{14}$$

Using saddle point approximation and comparing, order by order, with the expansion of the average plaquette from the strong coupling expansion [44], we can determine the expansion of $g(y)$. As in the case of $SU(2)$, there are logarithmic singularities at $y = \pm 1$, which can be subtracted by defining

$$h(y) \equiv g(y) - A \ln(1-y^2) \equiv \sum_{m=0} h_{2m} y^{2m} \ . \tag{15}$$

The value of A comes from the weak coupling expansion and will be discussed in the next subsection (see Eq. (20)). The infinite volume results are summarized in Table I. The entries make clear that as the order increases, the effect of the logarithmic subtractions becomes smaller. This indicates singularities closer to $y = 0$ ($s = 1$).

m	a_{2m}	g_{2m}	h_{2m}
1	$-\frac{1}{2}$	-1	$-\frac{3}{4}$
2	$\frac{1}{16}$	$-\frac{1}{4}$	$-\frac{1}{8}$
3	$-\frac{13}{96}$	$\frac{43}{36}$	$\frac{23}{18}$
4	$\frac{779}{6144}$	$-\frac{19}{192}$	$-\frac{7}{192}$
5	$-\frac{11819}{61440}$	$-\frac{7343}{1800}$	$-\frac{7253}{1800}$
6	$\frac{2017373}{847360}$	$\frac{465331}{25920}$	$\frac{466411}{25920}$
7	$-\frac{20224291}{123863040}$	$-\frac{983357143}{1693440}$	$-\frac{983296663}{1693440}$
8	$\frac{5775175013}{12683575296}$	$-\frac{201757201579}{46448640}$	$-\frac{201755750059}{46448640}$

TABLE I. U(1) strong coupling expansion coefficients a_{2m} of P (rescaled from Ref. [44]), and of $f(s)$ defined in the text.

The improvement of the approximation with successive order is shown in Fig. 3. The graph shows that for $s \gtrsim 0.5$, successive orders provide better approximations up to the point where the numerical accuracy is reached. Such a range corresponds to a convergent region $\beta \lesssim 0.9$ in the β-plane.

It should be noted that for the strong coupling expansion, the finite volume effects are negligible for $V = 8^4$.

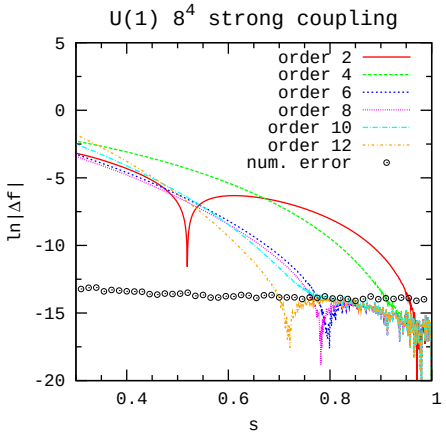

FIG. 3. Natural logarithm of the absolute value of the difference between $f(s)$ calculated on a 8^4 lattice and successive approximations obtained from the strong coupling expansion.

Indeed, they are even hard to resolve for $V = 4^4$. This can be traced to the fact [43] that even for this volume, the dependence on V would appear at order β^8 from the contributions of strong coupling graphs called torelons [45] that wrap around the periodic volume in one direction. As translations in that direction do not generate new graphs, such graphs have a suppression of order $1/L$ compared to graphs with a trivial topology. Consequently, for order less than 8, the finite volume effects can be estimated by canceling the volume dependence in the two terms of the r.h.s. of Eq. (13). For instance at lowest order, we find that

$$g_2 = -1 + 1/(8V) \ . \tag{16}$$

Consequently the difference $\Delta f(s)$ of $f(s)$ for two different volume V_1 and V_2 near $y = 0$ ($s = 1$) is

$$\Delta f(s) \simeq (1/8)(1/V_1 - 1/V_2)(s-1)^2 \ . \tag{17}$$

Even for $V = 4^4$, this difference is smaller than the error bars in the region $s \simeq 1$. In order to reduce the noise, we have averaged the data in bins of ten data points. The results are displayed in Fig. 4 which shows that the data and the analytical result in Eq. (17) are compatible.

D. Weak coupling

A similar approach can be followed in the weak coupling limit. At small s, the logarithmic singularity dominates and we assume that

$$f(s) = A \ln(s) + \sum_{m=0} f_m s^m \ . \tag{18}$$

The unknown coefficients can be determined from the weak coupling expansion of the average plaquette

$$P \simeq \sum_{m=1} b_m \beta^{-m} \ . \tag{19}$$

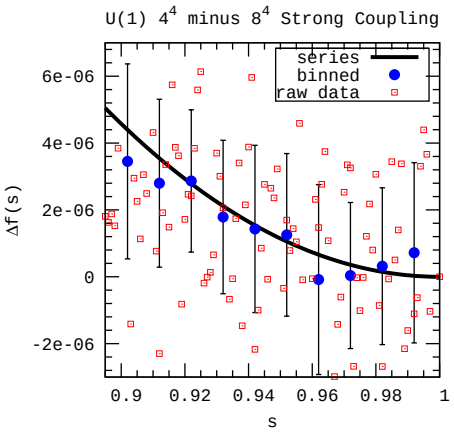

FIG. 4. Difference between $f(s)$ on 4^4 and 8^4 near s =1 (boxes). The circles are obtained by averaging over bins of size 10. The solid line is Eq. (17). The part with $s > 1$ can be obtained by symmetry and is not shown.

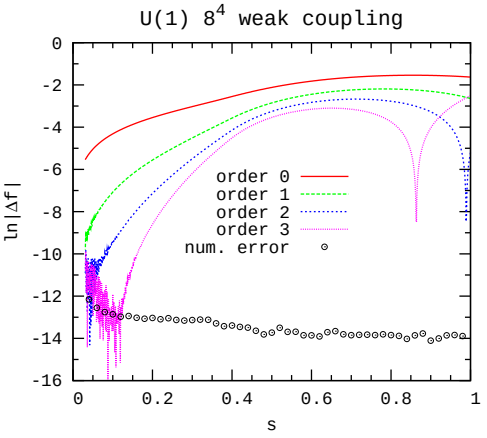

FIG. 5. Difference between $f(s)$ calculated on a 8^4 lattice and successive approximations obtained from the weak coupling expansion.

The volume dependent coefficients b_m have been calculated up to order 4 in Ref. [46]. The two lowest orders of the expansion can be performed exactly and yield:

$$A = 1/4 - 5/(12V) \ , \tag{20}$$

$$f_1 = (1/8)(1 - 1/V) \ . \tag{21}$$

The higher orders involve numerical loop calculations. The results of the expansion as well as the volume corrections for the 4^4 and 6^4 lattices are shown in Table II.

	$V=\infty$	$V=6^4$	$V=4^4$
b_1	$\frac{1}{4}$	$\frac{1295}{5184}$	$\frac{255}{1024}$
b_2	$\frac{1}{32}$	$\frac{2171747375}{208971104256}$	$\frac{65025}{2097152}$
b_3	0.01311	0.01309	0.01296
b_4	0.00752	0.00749	0.00739
A	$\frac{1}{4}$	$\frac{3883}{15552}$	$\frac{763}{3072}$
f_1	$\frac{1}{8}$	$\frac{1295}{10368}$	$\frac{255}{2048}$
f_2	0.07363	0.07359	0.07314
f_3	0.07638	0.07605	0.07515

TABLE II. The weak coupling expansion for $V = \infty$, 4^4 and 6^4. The upper half is the list of the expansion coefficients of the average plaquette P with respect to $1/\beta$ [46]. The lower half is the corresponding list of expansion coefficients of $f(x)$.

The difference between numerical and analytical results is shown in Fig. 5 for $V = 8^4$. The graph makes it clear that the quality of the approximation increases as three successive corrections to the leading logarithm are added. The third correction is good enough to reproduce the data within the numerical accuracy for $s < 0.1$. This order is not sufficient to identify a "non-perturbative envelope" defined in Ref. [47] and observed for $SU(2)$ in Ref. [43].

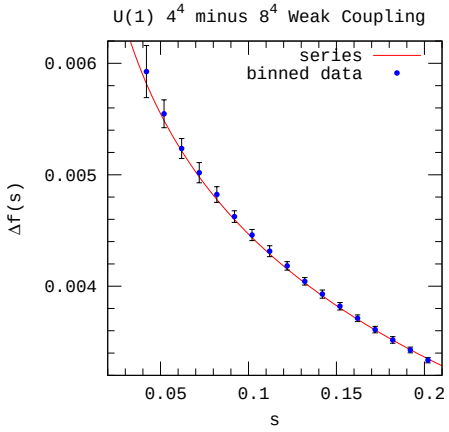

FIG. 6. Difference between $f(s)$ on 4^4 and 8^4 near $s = 0$ with average over bins of size 10. The solid line is the expansion described in the text.

The difference between $V = 4^4$ and $V = 8^4$ is shown in Fig. 6. Note that for the smallest volume ($V = 4^4$), the resolution in s used during the multicanonical simulation is coarser than the 1,000 bins used to represent $f(s)$. Consequently, some small "staircase" structure appears near 0 where $f(s)$ changes rapidly. For this reason, we have averaged $f(s)$ over bins of size 10 and Fig. 6 shows a good agreement with the analytical expansion that includes the logarithmic singularity and a linear term. Higher order corrections are significantly smaller than the errors bars. There is an arbitrary constant in the expansion of $f(x)$ which cannot be determined by the saddle point equation. For the numerical data, such a constant may differ for two different volumes and needs to be subtracted.

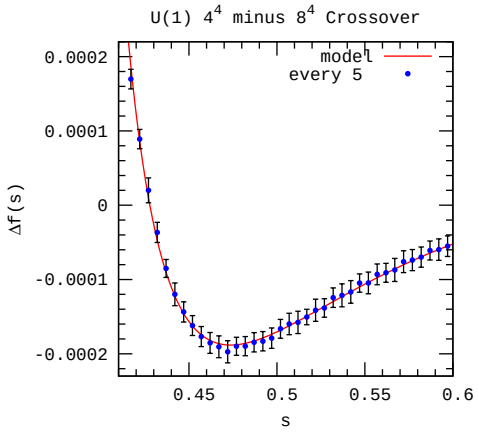

FIG. 7. Difference between $f(s)$ on 4^4 and 8^4 near $s = 0.5$. For readibilty, we only show every 5 points (no binning). The solid line is the fit given in Eq. (22).

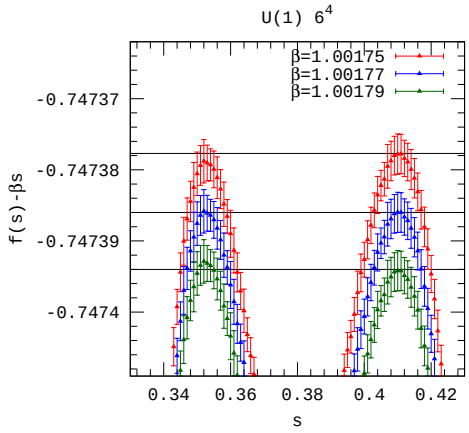

FIG. 8. $f(s) - \beta s$ for $\beta = 1.00175$, 100177 and 1.00179 on a 6^4 lattice. The horizontal lines have been drawn to emphasize small height asymmetries.

V. VOLUME DEPENDENCE IN THE CROSSOVER REGION

A. Empirical parametrization

The difference of $f(s)$ for 4^4 and 8^4 resembles the effective potential for the central Coulomb potential with a leading singularity near $s = 0.35$ and a $1/s$ behavior at larger s. Using in addition a constant that has no particular meaning as long as we don't normalize the density of states and a $1/s^2$ correction, we performed a 4-parameter fit with the 311 bins corresponding to $0.39 < s < 0.7$. The numerical result is:

$$f(s) = -0.00112063 + 4.82641 \times 10^{-6}/(-0.35+s)^2 - 0.000680501/s^2 + 0.00172882/s. \quad (22)$$

As shown in Fig. 7, it fits the data reasonably well.

B. Volume dependence of the double peak

The plaquette distributions for the volumes considered here have a double peak structure for β near 1. At finite volume, it is easy to locate the value of β, denoted β_S hereafter, where the two peaks of $f(s) - \beta_S s$ have equal height. Other pseudocritical β have been defined in the literature [30, 48–50]. The accuracy of the determination of β_S depends on the smoothness of the distribution and the size of the error bars. In Fig. 8, we show that $f(s) - \beta s$ is slightly tilted to the left for $\beta = 1.00175$ and to the right for $\beta = 1.00179$. Given the smoothness of the distribution, we conclude that $\beta_S = 1.00177(2)$. With the same graphs, we can also determine approximate values of the two maxima s_1 and s_2. The numerical results for the three volume considered are provided in Table III.

The density of states can be used to calculate the plaquette probability distribution at β_S. The results are shown in Fig. 9 where the normalization has been chosen in such a way that the integral under the curve is approximately one. Fig. 9 makes it clear that the dip between the peaks deepens and the peak separation decreases as the volume increases. This will be discussed in more detail in Sec. VII.

L	β_S	s_1	s_2
4	0.9793(1)	0.370(5)	0.445(5)
6	1.00177(2)	0.353(2)	0.411(2)
8	1.00734(1)	0.349(1)	0.395(1)

TABLE III. β_S, s_1 and s_2 defined in the text for $L = 4$, 6 and 8.

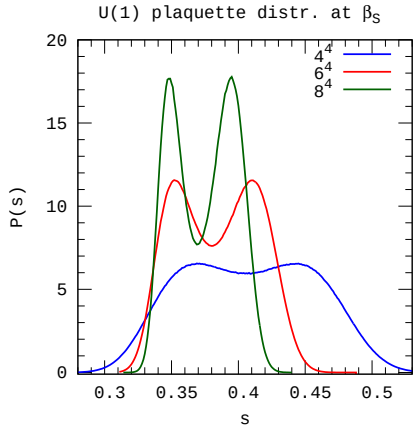

FIG. 9. Plaquette distribution for $U(1)$ at β_S for L= 4, 6 and 8.

VI. FISHER'S ZEROS

A. Approximate zeros from reweightings

Approximate values of Z at fixed β can be obtained by using the Riemann sum approximations of Eq. (4):

$$Z(\beta) \simeq \Delta s \sum_s \mathrm{e}^{\mathcal{N}_p(f(s)-\beta s)} \ . \tag{23}$$

We can now study how the error δf on $f(x)$ can affect our estimates of Z. The relevant quantity is $\mathcal{N}_p \delta f$ is included in Fig. 1. For the three volumes, $\mathcal{N}_p \delta f$ is of the order of a few percents and linearization is justified. Small scale fluctuations of the same order are visible in the distributions of the independent streams.

As we are interested in locating Fisher's zeros, it is clear that the errors have a potentially important effect near an approximate zero. The best we can do is to identify regions where $|Z|$ is significantly larger than $|\delta Z|$ so that we can confidently say that there are no zeros in these regions. If we use the linear estimate

$$\delta Z(\beta) \simeq \Delta s \sum_s \mathcal{N}_p \delta f(s) \mathrm{e}^{\mathcal{N}_p(f(s)-\beta s)} \ , \tag{24}$$

we have the inequality

$$|\delta Z(\beta)| < \Delta s \sum_s \mathcal{N}_p |\delta f(s)| \mathrm{e}^{\mathcal{N}_p(f(s)-Re\beta s)} \ , \tag{25}$$

but in general the bound is not sharp because the sign of $\delta f(s)$ can vary rapidly. We have estimated $|\delta Z|$ by taking the difference between Z calculated with the averaged f and Z calculated with the stream with the most tunnelings. The results are shown in Fig. 10. A mesh of 0.00025 in β is used which is larger than the typical fluctuations in f. The light (toward yellow on-line) regions represent the areas where we cannot exclude zeros. The dark (toward blue on-line) regions represent the areas where zeros are very unlikely. A small light region is an indication for the existence of a zero while a broad light region indicates that the errors dominate. The second possibility typically appears at large imaginary β where due to rapid oscillations of the integrand, cancellations occur making the final results more sensitive to the errors on $f(s)$. In view of this remark, Fig. 10 suggests that reweighting methods allow to estimate the locations of the two lowest zeros for $L = 4$ and three lowest zeros for $L = 6$.

We have also calculated ReZ and ImZ from Eq. (23) using the average f. Their respective zeros are shown in Fig. 11. The complex zeros appear at the intersections of the two sets of curves defined by ReZ=0 and ImZ=0 respectively. This happens in a way which is consistent with Fig. 10. Error bars can be estimated by comparing the intersections for the 20 streams. The results are given in Tables IV and V.

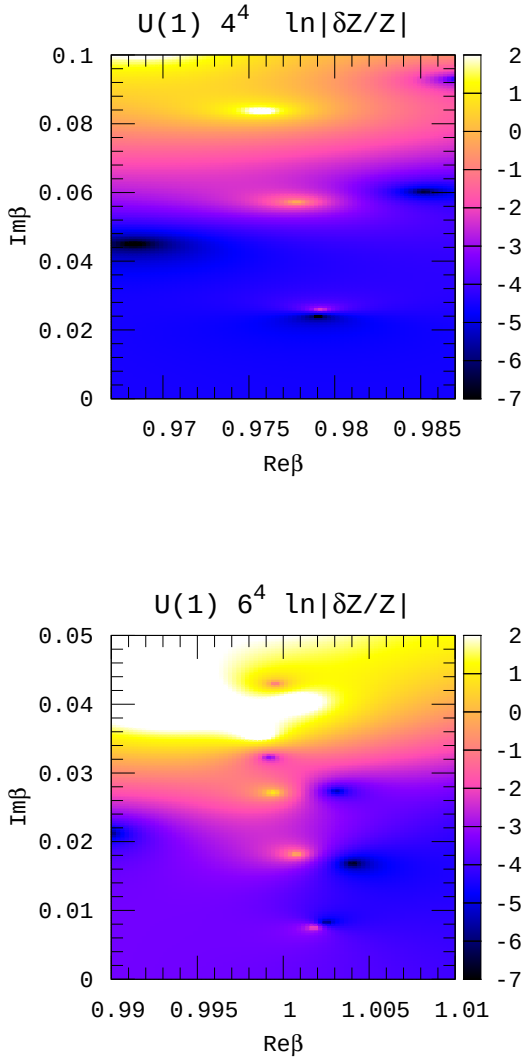

FIG. 10. $\ln|\delta Z/Z|$ for 4^4 and 6^4 lattices (color online).

L	first	second	third
4	0.9791(1)	0.9780(4)	not stable
6	1.00180(5)	1.0007(1)	0.9993(5)
8	1.00744(2)	1.0068(2)	1.0061(4)

TABLE IV. Real part of the first three zeros.

L	first	second	third
4	0.0259(1)	0.057(1)	not stable
6	0.00758(2)	0.018(1)	0.027(2)
8	0.00306(2)	0.008(1)	0.012(1)

TABLE V. Imaginary part of the first three zeros.

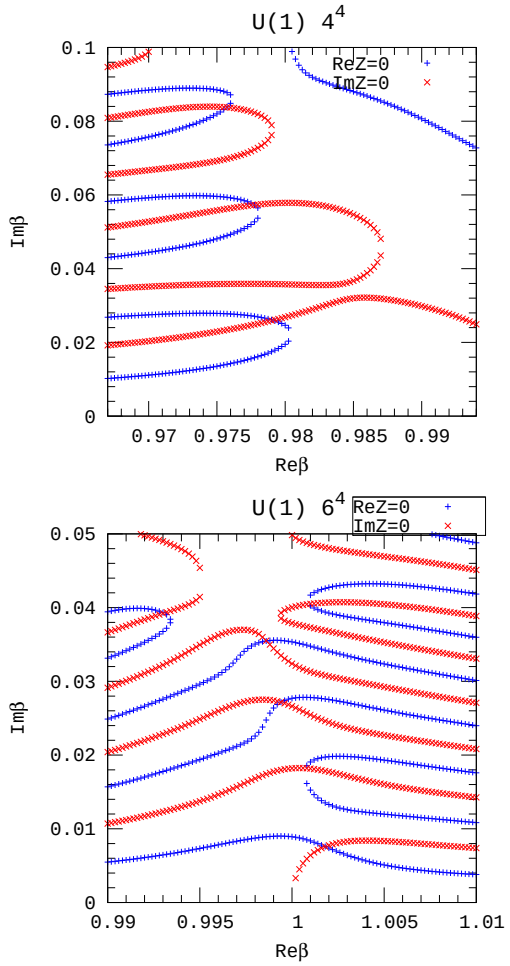

FIG. 11. Zeros of the Re (+, blue on-line) and Im (x, red on-line) part of Z for $U(1)$ using the density of states for 4^4 and 6^4 lattices.

B. Chebyshev interpolations

The original grids of the density of states are sometimes not sufficient for precise numerical integrations which is how we define our partition function. It is especially true when the imaginary component of β is large and, as a consequence, the partition function oscillates more frequently than the original grids can resolve. It is convenient to apply the Chebyshev interpolation which provides arbitrary integrating step sizes for designed integral precision. For the Chebyshev interpolation of numerical data, the determination of the coefficients by the Least Square Fit method is more efficient and robust than by discrete or integration methods. In this paper, we will primarily follow this approach.

A range of interest $[a, b]$ can be mapped to $[-1, 1]$ in which we express the target function by

$$f(y) = \sum_{n=0}^{N_c} c_n T_n(y) \ . \tag{26}$$

We then minimize the distance of the function to a data set or multiple data sets, which will uniquely determine the coefficients c_n of linear equations.

We shall keep in mind that, like other polynomial approximations, Chebyshev interpolations may introduce artifacts such as fake zeros. We want to make sure that the true zeros are distinct from the fake ones. Special attention should be paid to the range of approximation. In practice, we often use a small range to emphasize the numerical signal from a certain region. The average plaquette $\langle x \rangle$ is related to the coupling β, through $\langle x \rangle_\beta = -\partial \ln Z(\beta)/\partial\beta/\mathcal{N}_p$. This is not valid if $\langle x \rangle$ goes beyond the range of the approximation (an ellipse in the complex plane, see below). Reducing the range of interpolation may introduce fake zeros with large Imβ in the β complex plane. However the lowest zeros are usually not affected. Care should also be paid on the orders of the Chebyshev approximation. True zeros should be independent of the order of polynomials. In the following, we always use various orders of Chebyshev interpolations and make sure that the zeros are free of these artifacts.

C. Ellipse of convergence

The definition

$$T_n(z) = \cos(n \ \arccos(z)) \tag{27}$$

shows that the expansion in Chebyshev polynomials is a Fourier expansion for the variable $\arccos(x)$. If $|c_{n+1}/c_n|$ from Eq. (26) reaches a limit C, then the expansion converges for $|T_n(z)| < C^{-n}$. To work on the complex plane, the following relation is helpful: $T_n(z) = (\omega^n + \omega^{-n})/2$, when z is expressed as $z = (\omega + \omega^{-1})/2$. The convergence of a Chebyshev series is then analyzed through the variable ω. It can be shown [51] that the region of convergence on the ω-plane is a ring confined by a pair of concentric circles and the region is mapped into an area bounded by an ellipse on the z-plane.

The continuation of the Chebyshev expansion to the complex plane is limited by the ellipse. Fortunately, in the case of $U(1)$, the lowest complex zeros are typically very close to the real axis and these zeros are well inside the ellipse of convergence.

D. Locating zeros with the residue theorem

There is a general algorithm to find the zeros of an analytic function by using Cauchy's Integral Theorem [52]. For simplicity, we will only consider the special case when all the zeros are of order 1 which apparently applies to our problem. Suppose that an analytic function $Z(\beta)$ has K zeros enclosed by a closed contour C, then

$$\frac{1}{2\pi i} \oint_c (\ln Z)' \ \beta^n \ d\beta = \sum_{i=1}^{K} (\beta_i)^n, \quad n = 0, 1, 2, ... \tag{28}$$

L	Reβ	σ_s	σ_c	Imβ	σ_s	σ_c
	0.9791235	3.6e-5	5.3e-8	0.0260065	3.7e-5	3.9e-9
4	0.9777314	3.5e-4	7.1e-6	0.0572764	1.4e-4	3.3e-6
	0.9752954	1.1e-3	2.9e-4	0.0831705	1.3e-3	3.2e-4
	1.0017969	1.7e-5	1.7e-6	0.0075821	8.7e-6	1.4e-6
6	1.0007433	6.0e-5	2.3e-5	0.0182044	2.8e-5	4.0e-6
	0.9988964	1.4e-4	2.7e-4	0.0271866	4.5e-4	1.5e-4
	1.0074380	1.1e-5	7.7e-8	0.0030653	3.6e-6	6.8e-8
8	1.0068296	2.3e-5	2.1e-6	0.0077673	2.4e-5	3.3e-7
	1.0060410	1.1e-4	1.2e-5	0.0115079	1.0e-4	8.5e-5

TABLE VI. The lowest three zeros in the volumes 4^4, 6^4 and 8^4. Columns 2-4 are the real parts of the zeros, the estimate error σ_s from different streams of Monte Carlo runs and the error σ_c due to the orders of Chebyshev interpolation (we used three different orders 40, 44 and 50 for all three volumes). Columns 5-7 are similar quantities for the imaginary parts.

where β_i are all the zeros in contour C. When $n = 0$, the summation on the right hand side is just the number of zeros.

The partition function we are considering is an analytic function, since it is just a sum of analytic functions. We scan the complex plane with rectangular contours which enclose two or less zeros. We monitor the $n = 0$ integral which should give the number of zeros very close to an integer and a very small imaginary part. The method turns out to be quite robust and reliable.

E. Zero structure near the real axis

The lowest zeros from three volumes are given in Table VI and shown in Fig. 12. The error bars take into account both the Monte Carlo statistical error and the (much smaller) Chebyshev interpolation error. The three lines are the linear fits for the first, second and third lowest zeros. They intersect the real axis approximately at the same point $\beta = 1.01134(1)$. Fig. 12 also shows that β_S and the real part of the zeros are highly correlated.

The good look of the linear fits is deceptive as they have a rather large χ^2 and a small goodness of fit Q (see p. 111 of [53]) which can be explained by the small errors bars. Another potentially deceptive result is that the imaginary part of the lowest zero decreases like $L^{-3.08}$. If this result is indicative of what happens at larger volume, this would be interpreted as signaling a second order phase transition with $\nu \simeq 1/3.08 \simeq 0.325$. Larger lattices are needed as will be discussed in Sec. VII.

F. Dependence on the range of integration

In the previous calculations, the tails of integration play a marginal role. If we are interested only in the zeros near $\beta = 1$, the density of states in a finite range is sufficient. This information becomes very important at higher volumes where the calculation is more expensive. In Table VII, we provide the values s_a and s_b outside of which the knowledge of $f(s)$ has effects smaller than the error bars on the zeros.

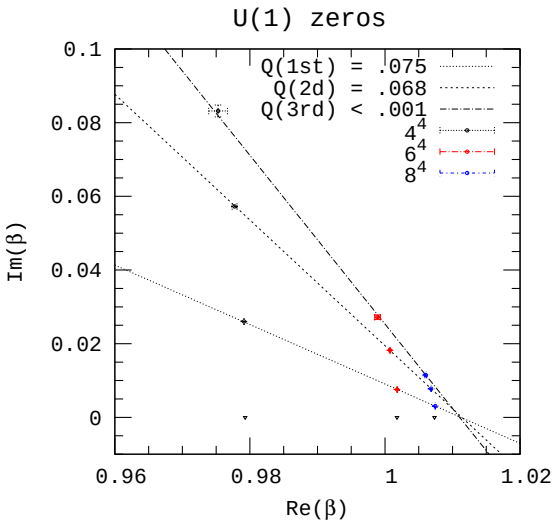

FIG. 12. The lowest zeros from the volumes 4^4, 6^4 and 8^4 (from left to right). Linear fits for the first, second and third zeros (bottom to top) and their goodness of fit Q. The diamonds on the real axis are the double-peak β's from Table III.

L	s_a	s_b	β_a	β_b
4	0.274	0.488	1.125	0.945
6	0.284	0.436	1.1	0.985
8	0.295	0.408	1.075	1

TABLE VII. Values of s_a and s_b and the corresponding values of β ($P(\beta) = s$).

VII. TOWARD LARGER VOLUME CALCULATIONS AND SCALING

In this section, we explore ways of discriminating between first and second order transitions. For this purpose, we include data at larger volumes (L=10, 12, 14 and 20) from Ref. [56] with much lower statistics, namely one stream with two MUCA runs.

A. Zeros

In Sec. VI, we explained that for the data for $L = 4$, 6 and 8, the imaginary part of the lowest zeros scales like $L^{-3.08}$. It is possible that as the volume increases, the approach of the real axis "rolls" toward the L^{-4} scaling

L	Reβ	$\Delta Re/2$	Imβ	$\Delta Im/2$
10	1.00947	2e-5	0.001478	2e-6
12	1.01027	2e-5	0.000795	2e-6
14	1.01064	2e-5	0.000449	8e-6
20	1.01101	1e-5	0.000119	1e-6

TABLE VIII. Higher volume zeros. Columns 2 and 4 are the averages over the two MUCA runs. Columns 3 and 5 are one half of the differences (not the estimated error, see text).

expected for a first order transition [30]. We now discuss the scaling of the zeros using the lower statistics data for the larger volumes given in Table VIII.

It is questionable that two MUCA runs could lead to a reliable estimate of the errors. An error bar from just two independent measurements fluctuates strongly and reaches a 95% confidence range only at about 14 (instead of 2) error bars (see p.78 of [53]). We decided therefore to smoothen the error bars by assuming that the real relative error is the same for all four of our large lattices. Averaging these relative errors and multiplying the by three, the approximate 95% confidence range of four independent data, gives an error bar of 1.69%, which is then given in the fourth column for all the large data of of Table IX. Not to overweight the far more accurate small lattice against the large lattice data in the subsequent fits, they are also used with a relative error of 1.69% and thus listed in Table IX. We want to emphasize that this procedure has been designed to understand how different fits allow to discriminate between first and second order rather than to extract accurate values for the fitted parameters.

L	First Run	Second Run	Combined
4	–	–	0.02691 (44)
6	–	–	0.00758 (13)
8	–	–	0.003065 (52)
10	0.0014756	0.0014797	0.001478 (25)
12	0.0007927	0.0007969	0.000795 (14)
14	0.00045747	0.00044157	0.0004495 (76)
20	0.000011882	0.000011901	0.00001189 (21)

TABLE IX. y = Imz from two independent runs on $L \geq 10$ lattices and their combination as explained in the text together with reduced accuracy values from $L \leq 8$ lattices.

For these data we performed 3-parameter fits, which are listed in the following together with their goodness

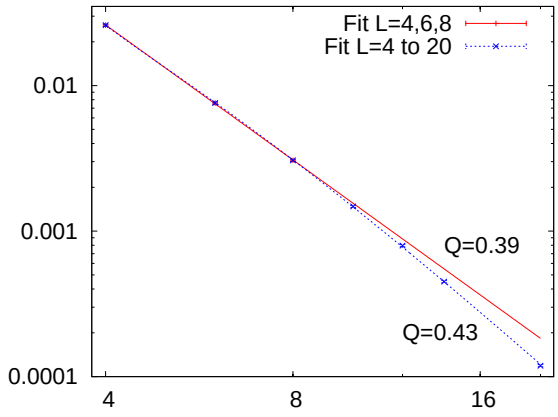

FIG. 13. Fits of Im$z(L)$ on a log-log scale.

of fit Q.

$$y = \frac{a_1}{L^4}\left(1 + \frac{a_2}{L} + \frac{a_3}{L^2}\right), \quad Q = 0.43\,, \tag{29}$$

$$y = a_1 L^{a_2}\left(1 + \frac{a_3}{L}\right), \quad Q = 6.2 \times 10^{-4}\,, \tag{30}$$

$$y = \frac{a_1}{L^4}\left(1 + a_2 L^{a_3}\right), \quad Q = 2.8 \times 10^{-3}\,. \tag{31}$$

The first fit shows that L^{-4} behavior is consistent with all the data put together. The other two fits are in disagreement with the data.

Using *only* the data from the $L = 4$, 6, 8 lattices with the *modified* error bars given in Table IX, the 2-parameter fit

$$y = a_1\, L^{a_2}\,, \quad Q = 0.39 \tag{32}$$

is also in agreement with the data and gives the exponent $a_2 = -3.082\,(35)$ instead of -4. The fits (29) and (32) are shown in Fig. 13.

However, the fit

$$y = \frac{a_1}{L^{3.08}}\left(1 + \frac{a_2}{L} + \frac{a_3}{L^2}\right), \tag{33}$$

with the seven data points leads to $Q < 10^{-8}$. In addition, if we perform a four parameter fit as in Eqs. (29) and (33) but with the leading exponent fitted, we obtain 4.121(74) for this exponent with Q=0.72. These results seem to favor the first order possibility. However, they should be checked with higher statistics data for the larger volumes.

B. Features of $f(s)$

In the infinite volume limit, the width of the double peak distribution goes to a nonzero limit (latent heat) for a first order phase transition. For a second order transition, this width should go to zero as an inverse power of L. These two possibilities are tested by plotting the width versus $1/L$ or in a log-log scale in Fig. 14.

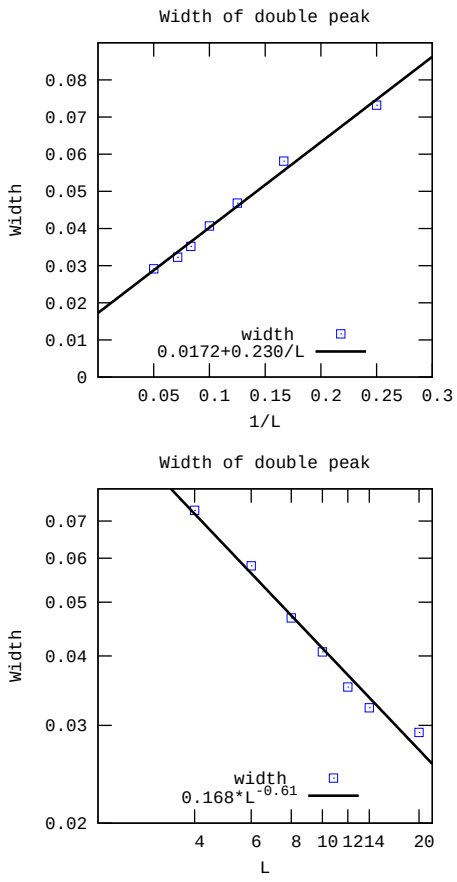

FIG. 14. Width of $f - \beta_S s$ as a function of L.

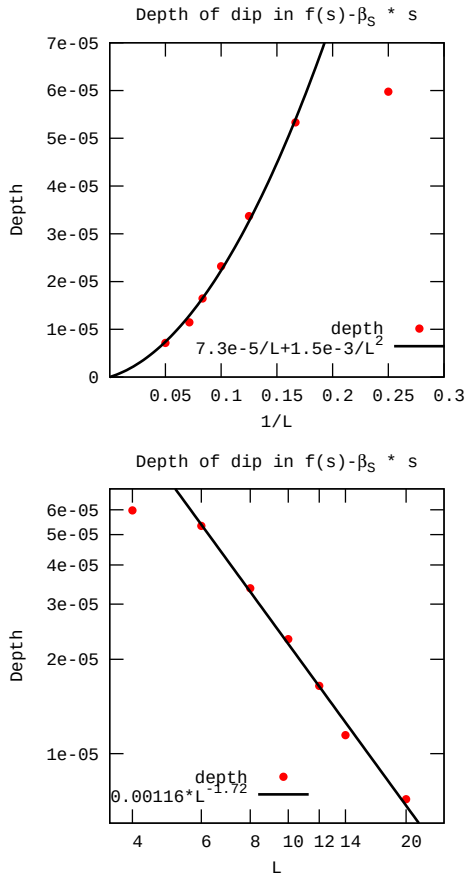

FIG. 15. Difference between the local minimum and the local maxima of $f - \beta_S s$ as a function of L.

The difference between the local minimum and the local maxima of $f - \beta_S s$ (by definition of β_S, the two local maxima have the same height) should decay like C/L for a first order transition with C proportional to the interface tension. For a second order transition, this difference should go to zero as an inverse power of L. The data is shown versus $1/L$ and on a log-log scale together with simple fits (made without $L = 4$) in Fig. 15. In the first fit, the $1/L^2$ corrections are clearly important and it is not surprising that the power in the second fit is between -1 and -2.

Using arguments from Ref. [54], leads to the conclusion that for a second order phase transition, the width should scale like $L^{-(1-\alpha)/\nu}$, while the depth should scale like L^{-D}. If we use $D = 4$, $\nu \simeq 0.325$ and the hyperscaling relation $\alpha = 2 - D\nu \simeq 0.7$, we obtain $(1 - \alpha)/\nu \simeq 0.92$ which is not too far off for the width but very far off for the depth.

VIII. CONCLUSION

Using multicanonical methods we have calculated the density of states for pure $U(1)$ lattice gauge theory with high precision on small 4^4, 6^4 and 8^4 lattices and with moderate precision on larger 10^4, 12^4, 14^4 and 20^4 lattices. From these data we were able to locate low-lying Fisher's zeros by Chebyshev interpolations and residue theorem methods. On the small lattices the scaling properties of the zeros are consistent with a second order phase transition, while from the larger lattices there is some indication that this turns around and becomes consistent with a first order transition.

Although $U(1)$ lattice gauge theory was already introduced in the pioneering paper by Wilson [55], it still resists to reveal clearly the true nature of its transition from the confinement to the Coulomb phase. Like other physical quantities, e.g., Polyakov loop susceptibilities, Fisher's zeros appear to need rather large lattices to display their asymptotic scaling properties. As modern supercomputers allow parallel processing on an unprecedented scale, the solution may finally become achieved by brute force calculations on very large lattices.

ACKNOWLEDGMENTS

This research was supported in part by the Department of Energy under Contracts No. FG02-91ER40664, DE-

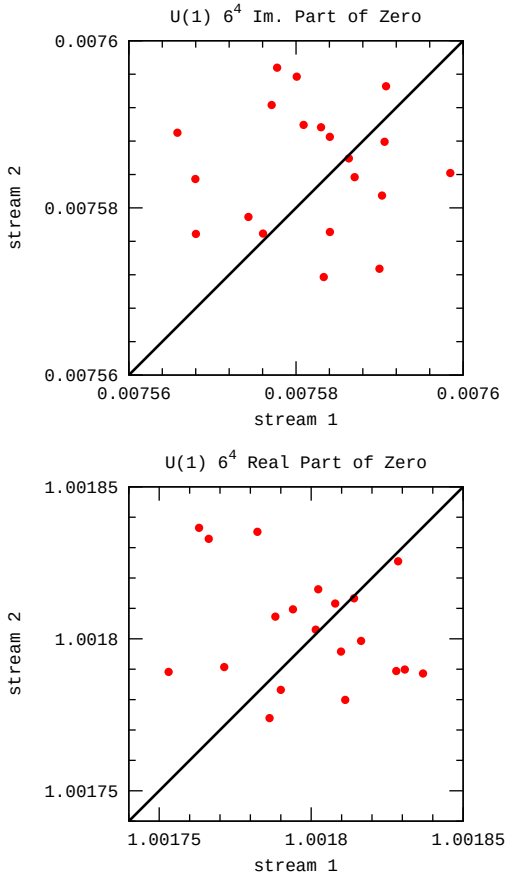

FIG. 16. Imaginary (top) and Real (bottom) part of the complex zeros of MUCA run 1 versus MUCA run 2 for the 20 streams on a 6^4 lattice.

FG02-97ER41022 and DE-AC02-98CH10886. We thank C. Bender for pointing out the concept of Chebyshev ellipses and W. Jancke for providing unpublished figures of double-peak distributions in a case of second order phase transition. The calculations were supported in part by a project of level C on the Fermilab cluster.

Appendix A: Multicanonical data

The number of tunnelings and the integrated autocorrelation times for 4^4, 6^4 and 8^4 lattices is given in Tables X-XII. Fig. 16 illustrates the fluctuations among streams and the correlations among MUCA runs for the zeros on a 6^4 lattice. In table XIII we summarize the parameters of simulations on 10^4–20^4 lattices.

Appendix B: Numerical data used in Sec. VII

In order to calculate the quantities used to make the graphs of Sec. VII, we have first fitted $f(s)$ in a region slightly wider than the location of the two peaks

	MUCA 1	MUCA 2		MUCA 3	
#	N^{tunn}	N^{tunn}	τ_{int}	N^{tunn}	τ_{int}
1	1,512	3,886	99(2)	4,697	110(1)
2	1,406	4,018	109(1)	2,833	720(35)
3	1,974	4,723	114(5)	3,492	540(15)
4	1,552	4,537	216(5)	2,684	750(18)
5	774	5,038	175(12)	4,920	367(29)
6	963	4,769	109(1)	5,682	164(4)
7	196	397	1383(124)	3,162	679(34)
8	4,089	3,875	101(5)	4,547	116(5)
9	2,344	4,214	108(7)	4,599	266(6)
10	1,652	4,582	185(15)	3,484	625(48)
11	1,622	4,179	111(7)	5,030	255(12)
12	1,722	4,281	126(3)	3,985	674(101)
13	3,406	4,081	98(1)	4,994	146(3)
14	1,271	4,127	104(6)	5,257	135(6)
15	488	4,610	255(9)	3,776	524(14)
16	2,351	4,394	108(3)	4,167	338(12)
17	788	4,785	123(4)	4,598	356(10)
18	735	4,680	134(4)	4,661	364(16)
19	845	4,450	200(4)	3,675	537(14)
20	2,697	3,526	93(1)	4,123	104(7)

TABLE X. MUCA data for 4^4.

	MUCA 1		MUCA 2	
#	N^{tunn}	τ_{int}	N^{tunn}	τ_{int}
1	1,351	702(48)	950	559(27)
2	708	466(12)	897	480(11)
3	367	422(12)	947	502(17)
4	454	474(30)	971	561(31)
5	580	484(37)	894	565(47)
6	682	481(21)	911	511(23)
7	523	423(14)	909	557(43)
8	765	512(28)	903	532(33)
9	696	510(27)	921	485(12)
10	652	469(32)	935	569(53)
11	513	544(46)	976	523(33)
12	378	396(18)	976	536(27)
13	867	559(17)	961	495(10)
14	661	496(13)	932	509(28)
15	545	542(50)	896	554(38)
16	615	497(14)	920	496(13)
17	475	438(16)	979	543(46)
18	822	464(10)	903	486(11)
19	878	570(35)	892	508(30)
20	578	588(62)	949	572(28)

TABLE XI. MUCA data for 6^4.

L	β_S	s_1	s_2	$\Delta(f-\beta_S s)$	s_L	s_R	β_L	β_R	$\beta_R-\beta_L$
4	0.979327	0.369215	0.442409	0.0000597527	0.384952	0.425551	0.976759	0.981792	0.00503262
6	1.00176	0.352413	0.410538	0.0000533197	0.364762	0.395541	0.998768	1.00446	0.00569344
8	1.00738	0.348089	0.394932	0.0000337064	0.358049	0.382876	1.00504	1.00951	0.00447297
10	1.00942	0.345567	0.386254	0.000023194	0.353401	0.37509	1.00747	1.01103	0.00356233
12	1.01022	0.345633	0.380806	0.0000164495	0.352382	0.370685	1.0086	1.01153	0.00293064
14	1.01058	0.345352	0.377624	0.0000114541	0.351326	0.368136	1.00934	1.01155	0.00221252
20	1.01097	0.345337	0.374469	$7.1542782\ 10^{-6}$	0.349468	0.36223	1.00988	1.01157	0.0016911

TABLE XIV. Numerical results described in the text.

	MUCA 1		MUCA 2	
#	N^{tunn}	τ_{int}	N^{tunn}	τ_{int}
1	145	1,756(99)	252	1,782(124)
2	79	1,298(69)	240	1,798(78)
3	75	1,475(144)	259	2,486(368)
4	121	1,291(141)	216	2,159(235)
5	150	2,420(364)	216	1,660(154)
6	86	1,097(40)	256	1,528(55)
7	74	1,103(51)	255	1,621(105)
8	132	1,419(48)	254	1,568(98)
9	187	3,089(438)	197	3,074(397)
10	98	1,370(94)	255	1,706(104)
11	142	1,389(47)	208	1,700(218)
12	165	1,804(343)	254	1,800(256)
13	93	1,265(111)	270	1,912(160)
14	212	2,012(114)	231	1,855(254)
15	137	1,581(181)	249	1,855(170)
16	159	1,904(235)	211	1,674(224)
17	269	1,773(76)	213	2,169(256)
18	206	1,773(176)	234	1,503(52)
19	214	1,756(76)	212	1,954(265)
20	96	1,680(221)	227	1,697(101)

TABLE XII. MUCA data for 8^4.

volume	sweeps	β_{min}	β_{max}	MUCA1	MUCA2
10^4	$32\times 96,000$	0.980	1.030	103	133
12^4	$32\times 112,000$	0.990	1.030	75	82
14^4	$32\times 128,000$	1.000	1.020	57	51
20^4	$64\times 100,000$	1.010	1.012	155	210

TABLE XIII. MUCA data for volumes where simulations were performed in narrow $[\beta_{min},\beta_{max}]$ range. Last two columns summarize the number of tunneling events. 10^4 – 12^4. is from [56].

of $f(s)-\beta_S$ with the first 12 Chebyshev polynomials. Higher order polynomials tend to pick up the noise and provide results which are less stable. Using this polynomial approximation, we calculated the two roots of $f''(s)$ in the interval considered. We call them s_L (Left) and s_R (Right). They are the local extrema of $f'(s)$. The corresponding β (obtained from the saddle point Eq. (12) are denoted β_L and β_R. For $\beta_L<\beta<\beta_R$, the saddle point Eq. (12) has three solutions instead of one (the "Maxwell kink"). β_S corresponds to the case where the area of the kink below and above are equal. The location of the maxima of $f(s)-\beta_S s$ are called s_1 and s_2 as in Sec. V. $\Delta(f-\beta_S s)$ denotes the difference between the local minimum and the local maxima of $f-\beta_S s$. The numerical results are provided in Table XIV.

[1] T. Appelquist, G. T. Fleming, and E. T. Neil, Phys. Rev. D **79**, 076010 (2009), arXiv:0901.3766 [hep-ph].

[2] A. Hasenfratz, Phys. Rev. D **80**, 034505 (2009), arXiv:0907.0919 [hep-lat].

[3] Z. Fodor, K. Holland, J. Kuti, D. Nogradi, and C. Schroeder, Phys. Lett. B **681**, 353 (2009), arXiv:0907.4562 [hep-lat].

[4] A. Deuzeman, M. P. Lombardo, and E. Pallante, Phys. Rev. D **82**, 074503 (2010), arXiv:0904.4662 [hep-ph].

[5] Z. Fodor, K. Holland, J. Kuti, D. Nogradi, and C. Schroeder, Phys. Lett. B **703**, 348 (2011), arXiv:1104.3124 [hep-lat].

[6] A. Hasenfratz, Phys. Rev. D **82**, 014506 (2010), arXiv:1004.1004 [hep-lat].

[7] Y. Shamir, B. Svetitsky, and T. DeGrand, Phys. Rev. D **78**, 031502 (2008), arXiv:0803.1707 [hep-lat].

[8] J. B. Kogut and D. K. Sinclair, Phys. Rev. D **81**, 114507 (Jun. 2010), arXiv:1002.2988 [hep-lat].

[9] T. DeGrand, Y. Shamir, and B. Svetitsky, Phys. Rev. D **83**, 074507 (2011), arXiv:1102.2843 [hep-lat].

[10] D. K. Sinclair and J. . B. Kogut, PoS **LATTICE2010**, 071 (2010), arXiv:1008.2468 [hep-lat].

[11] J. B. Kogut and D. K. Sinclair(2011), arXiv:1105.3749 [hep-lat].

[12] L. Del Debbio and R. Zwicky, Phys. Rev. D **82**, 014502 (2010), arXiv:1005.2371 [hep-ph].

[13] J. C. Myers and M. C. Ogilvie, JHEP **07**, 095 (2009), arXiv:0903.4638 [hep-th].

[14] T. DeGrand, Phil. Trans. R. Soc. A **369**, 2701 (2011), arXiv:1010.4741 [hep-lat].

[15] M. C. Ogilvie, Phil. Trans. R. Soc. A **369**, 2718 (2011), arXiv:1010.1942 [hep-lat].

[16] F. Sannino, Acta Phys. Polon. B **40**, 3533 (2009), arXiv:0911.0931 [hep-ph].

[17] B. A. Berg, Phys. Rev. **D82**, 114507 (2010), arXiv:1011.6406 [hep-lat].

[18] B. A. Berg(2011), arXiv:1109.5861 [hep-lat].

[19] A. Denbleyker, D. Du, Y. Liu, Y. Meurice, and H. Zou, Phys. Rev. Lett. **104**, 251601 (2010), arXiv:1005.1993 [hep-lat].

[20] Y. Meurice and H. Zou, Phys. Rev. D **83**, 056009 (Mar. 2011), arXiv:1101.1319 [hep-lat].

[21] Y. Liu and Y. Meurice, Phys. Rev. D **83**, 096008 (2011), arXiv:1103.4846 [hep-lat].

[22] E. T. Tomboulis, Mod. Phys. Lett. A **24**, 2717 (2009).

[23] M. Fisher, "in lectures in theoretical physics vol. viic," (University of Colorado Press, Boulder, Colorado, 1965).

[24] N. A. Alves, B. A. Berg, and S. Sanielevici, Phys. Rev. Lett. **64**, 3107 (1990).

[25] J. Jersak, C. B. Lang, and T. Neuhaus, Phys. Rev. Lett. **77**, 1933 (1996), arXiv:hep-lat/9606010.

[26] J. Jersak, C. Lang, and T. Neuhaus, Phys.Rev. D **54**, 6909 (1996), arXiv:hep-lat/9606013 [hep-lat].

[27] W. Janke and R. Kenna, J. Stat. Phys. **102**, 1211 (2001), cond-mat/0012026.

[28] W. Janke and R. Kenna, Nucl. Phys. Proc. Suppl. **106**, 905 (2002), hep-lat/0112032.

[29] W. Janke, D. A. Johnston, and R. Kenna, Nucl. Phys. **B682**, 618 (2004), cond-mat/0401097.

[30] B. Klaus and C. Roiesnel, Phys. Rev. D **58**, 114509 (1998), arXiv:hep-lat/9801036.

[31] I. Campos, A. Cruz, and A. Tarancon, Nucl.Phys. **B528**, 325 (1998), arXiv:hep-lat/9803007 [hep-lat].

[32] G. Arnold, T. Lippert, K. Schilling, and T. Neuhaus, Nucl.Phys.Proc.Suppl. **94**, 651 (2001), arXiv:hep-lat/0011058 [hep-lat].

[33] G. Arnold, B. Bunk, T. Lippert, and K. Schilling, Nucl. Phys. Proc. Suppl. **119**, 864 (2003), arXiv:hep-lat/0210010.

[34] M. Vettorazzo and P. de Forcrand, Nucl.Phys. **B686**, 85 (2004), arXiv:hep-lat/0311006 [hep-lat].

[35] B. A. Berg and T. Neuhaus, Phys. Lett. **B267**, 249 (1991).

[36] F. Wang and D. P. Landau, Phys. Rev. Lett. **86** (2001).

[37] A. Bazavov and B. A. Berg, Phys. Rev. D **71**, 114506 (2005), arXiv:hep-lat/0503006.

[38] A. Bazavov and B. A. Berg, Comput. Phys. Commun. **180**, 2339 (2009), arXiv:0903.3984 [hep-lat].

[39] A. Denbleyker, D. Du, Y. Meurice, and A. Velytsky, PoS **LAT2007**, 269 (2007), arXiv:0710.5771 [hep-lat].

[40] N. A. Alves, B. A. Berg, and R. Villanova, Phys. Rev. B **41**, 383 (1990).

[41] N. A. Alves, B. A. Berg, and S. Sanielevici, Nucl. Phys. **B376**, 218 (1992), hep-lat/9107002.

[42] L. Li and Y. Meurice, Phys. Rev. D **71**, 016008 (2005), hep-lat/0410029.

[43] A. Denbleyker, D. Du, Y. Liu, Y. Meurice, and A. Velytsky, Phys. Rev. D **78**, 054503 (2008), arXiv:0807.0185 [hep-lat].

[44] R. Balian, J. M. Drouffe, and C. Itzykson, Phys. Rev. D **19**, 2514 (1979).

[45] C. Michael and M. Teper, Nucl. Phys. **B314**, 347 (1989).

[46] R. Horsley and U. Wolff, Phys. Lett. **B105**, 290 (1981).

[47] Y. Meurice, Phys. Rev. D **74**, 096005 (2006), arXiv:hep-lat/0609005.

[48] C. Borgs, R. Kotecký, and S. Miracle-Solé, Journal of Statistical Physics **62**, 529 (Feb. 1991).

[49] C. Borgs and R. Kotecký, Journal of Statistical Physics **61**, 79 (Oct. 1990).

[50] A. Billoire, T. Neuhaus, and B. Berg, Nucl. Phys. **B396**, 779 (1993), arXiv:hep-lat/9211014.

[51] J. P. Boyd, Journal of Scientific Computing **3**, 109 (1998).

[52] P. Kravanja, M. Van Barel, O. Ragos, M. Vrahatis, and F. Zafiropoulos, Computer Physics Communications **124**, 212 (Feb. 2000).

[53] B. Berg, *Markov Chain Monte Carlo Simulations and Their Statistical Analysis* (World Scientific, Singapore, 2004).

[54] H. Behringer and M. Pleimling, Phys. Rev. E **74**, 011108 (Jul 2006).

[55] K. G. Wilson, Phys. Rev. D **10**, 2445 (1974).

[56] B. A. Berg and A. Bazavov, Phys. Rev. D **74**, 094502 (2006), arXiv:hep-lat/0605019.